Nanoscale

Supplementary Information

Cobalt selenide with ordered cation vacancies for efficient oxygen reduction and frigostable Al-air batteries

Jianxue Liu,*[a,b] Chao Zhang,[a] Chen Xu,[c] Wenwen Yang,[d] Yuan Cao[e] and Huimin Lu*[b]

[a]Aerospace Research Institute of Materials & Processing Technology, Beijing, 100076, China.

[b]School of Materials Science and Engineering, Beihang University, Beijing 100191, China.

[c]Jinan Yihang New Material Technology Co., Ltd., Jinan 271100, China.

[d]School of Basic Education, Beijing Polytechnic College, Beijing 100042, China.

[e]School of Energy and Power Engineering, Beihang University, Beijing 100191, China.

* *Corresponding author. Tel/Fax: 010-69075668.*

E-mail address: lhm0862002@aliyun.com (Prof. Huimin Lu)

ljx1654060931@foxmail.com (Jianxue Liu)

1. Experiment

1.1. Catalyst synthesis

ZIF-67 nanocubes were fabricated by a surfactant-modified aqueous-solution method. Cobalt nitrate hexahydrate ($Co(NO_3)_2 \cdot 6H_2O$, 99%, Aladdin, 700 mg) and cetyltrimethylammonium bromide (CTAB, 99%, Aladdin, 5 mg) were dissolved into deionized water (DIW, 10 mL); 2-methylimidazole (2-MEIM, 98%, Alfa, 15 g) was also dissolved into DIW (100 mL). Then these solutions ware mixed and magnetically stirred for 1 h at room temperature (RT). Finally, this purple suspension was centrifuged, and washed 3 times with DIW, and dried for standby.

Polyacrylonitrile (PAN, Mw = 150,000, Aladdin, 0.55 g) powder was dissolved in N,N-dimethyformamide (DMF, 99.9%, Alfa, 5.5 mL) before ZIF-67 (0.2 g) was mixed into the precursor violently. This solution was electrospun by a propulsion rate of 1 mL h^{-1} with a voltage of 12-13 kV. The needle tip was distanced at 10-13 cm from the collector (25 cm × 30 cm).

The purple interwoven mat was hold at 280 °C for 1 h in air by a heating rate of 2 °C min^{-1} in a tube furnace. Afterwards, selenium (Se, ⩾99.99%, Alfa) was laid at the bottom of an alumina boat under an equal weight of the heat treated mat. They were reheated to 800 °C at a rate of 2 °C min^{-1} and rested for another 2 h in H_2/Ar (5 vol. %) to produce $Co_{0.85}Se$@N,Se-CNFs. As contrast, ZIF-67 precipitation was ground with Se powder and directly carbonized/selenized with the identical parameters to obtain $Co_{0.85}Se$/C; PAN nanofibers electrospun without ZIF-67 were also stabilized in air before carbonized/selenized with the same conditions to achieve N,Se-CNFs. Raw ZIF-67 was carbonized at 800 °C for 2 h in H_2/Ar (5 vol. %) to produce Co/C. The white mat electrospun by only PAN/DMF and the purple mat from PAN/DMF with ZIF-67 were stabilized in air before carbonization with the same conditions to fabricate N-CNFs and Co@N-CNFs.

1.2. Material characterization

Powder X-ray diffraction (PXRD) spectrums were obtained by a Bruker D8 Advace X-Ray Diffractometer to determine the phase compositions of these samples. Scanning electron microscopy (SEM) characterizations were processed using a su8020 microscope to finish the microstructure analysis. Transmission electron microscopy (TEM) pictures were achieved by FEI Tecnai G2F30 to analyze the morphology, element distribution. Moreover, the selected area electron diffraction (SAED) pattern was taken to confirm the chemical composition of the NPs in the carbon matrix. The chemical state of those elements were characterized using XPS spectra on Thermo ESCAlab 250XI. The work function and band edges of the samples were determined by UPS which was performed on the same instrument as XPS using He I ($h\upsilon$ = 21.22 eV) excitation source at an applied bias voltage of 5 V and 0 V. The values of work function were calculated using the equation:

$$\Phi = h\upsilon - |E_{cut} - E_F|$$

Φ is the work function. h is the Planck constant($6.62606957(29)\times10^{-34}$J·s) and $h\upsilon$ (21.22 eV) represents the incident photoenergy from He I excitation source. E_F is the Fermi edge. E_{cut} is the secondary electron cutoff level. The optical properties of $Co_{0.85}$Se@N,Se-CNFs, $Co_{0.85}$Se/C and Co@N-CNFs were measured by UV-vis spectrometry (Hitachi U3900).

Thermal weight loss was measured by thermogravimetric analysis (TGA) on a METTLER TGA/DSC 1SF/1382 instrument to conduct the thermal decomposition analysis. The S_{BET} and pore structure were examined by nitrogen adsorption-desorption isotherms on the Micromeritics Apparatus (TriStar II3020) to describe their surface.

1.3. ORR tests

Electrochemical tests were conducted using a MSRX system with a 3-electrode configuration.

A Hg/HgO electrode worked as the reference, a square Pt plate (2 cm × 2 cm) as the counter, while 0.1 M KOH aqueous solution saturated with O_2 as the electrolyte. The glass carbon electrode (Φ5 mm) was set as the working electrode. These patterns were plotted by Gamry Reference 3000.

To prepare the working electrode, $Co_{0.85}Se$@N,Se-CNFs was efficiently ground with acetylene black with a weight ratio of 1:1. Then 20 mg of this mixture was poured into a solution of ethanol (1 mL), water (1 mL) and Nafion solution (5 wt. %, Alfa Aesar, 25 μL) before it was energetically sonicated. 10 μL of this black suspension liquid was dripped on a glass carbon electrode and incubated overnight at RT. The cyclic voltammetry (CV) curves were scanned between -1.0 V and 0.1 V (vs Hg/HgO). The linear sweep voltammetry (LSV) curves were recorded between -0.8 V and 0.1 V (vs Hg/HgO) at 10 mV s^{-1}. The beginning potential of ORR was characterized as 5% of the diffusion-limited current density[1]. Pt/C was also measured as the benchmark. The electron quantity (n) transferring in ORR was computed relating to Koutecky-Levich formulas:

$$1/j=1/j_k + 1/B\omega^{1/2} \quad (1)$$

$$j_k = nFkC_0 \quad (2)$$

$$B =0.62nFD_0^{2/3}\, v^{-1/6}\, C_0 \quad (3)$$

where j stands for the measured current density during ORR, j_k for the kinetic current density, ω for the angular velocity of the disc, F for the Faraday constant (96485 C mol^{-1}), C_0 for the bulk saturation concentration of O_2 in the alkali solution (1.2×10^{-6} mol cm^{-3}), k for a constant of electronic transmission rate and B for the slope reciprocal; and D_0 symbolizes the diffusion coefficient of the dissolved O_2 in 0.1 M KOH (1.9×10^{-5} cm^2 s^{-1}), v describes the kinematic viscosity of the alkali solution (0.01 cm^2 s^{-1}). The potential value vs reversible hydrogen electrode (RHE) was calculated from the referred potential vs Hg/HgO by the formula:

$$E_{(RHE)} = E_{(Hg/HgO)} + E^{\theta}_{(Hg/HgO)} + 0.0591 \times pH \quad (4)$$

where pH relates to the 0.1 M KOH solution and $E^{\theta}_{(Hg/HgO)}$ symbolizes the standard potential of Hg/HgO/0.1 M KOH at RT (0.164 V vs. RHE).

The ORR activity was also evaluated by RRDE in O_2-saturated 0.1 M KOH solutions at room temperature. The peroxide percentage and the transferred electron number (n) were calculated based on the following equations:

$$\%HO_2^- = 200 \times I_r/N/(I_d + I_r/N) \quad (5)$$

$$n = 4 \times I_d/(I_d + I_r/N) \quad (6)$$

where I_d is the disk current, I_r is the ring current, and N is the current collection efficiency of the Pt ring with a value of 0.37.

1.4. XAFS measurements

The X-ray absorption fine structure spectra (XAFS) were collected at 1W1B station in Beijing Synchrotron Radiation Facility (BSRF). The storage rings of BSRF was operated at 2.5 GeV with an average current of 250 mA. Using Si(111) double-crystal monochromator, the data collection were carried out in transmission/fluorescence mode using ionization chamber. All spectra were collected in ambient conditions.

1.5. XAFS Analysis and Results

The acquired EXAFS data were processed according to the standard procedures using the ATHENA module implemented in the IFEFFIT software packages. The k^3-weighted EXAFS spectra were obtained by subtracting the post-edge background from the overall absorption and then normalizing with respect to the edge-jump step. Subsequently, k^3-weighted $\chi(k)$ data of Co K-edge were Fourier transformed to real (R) space using a hanning windows (dk=1.0 $Å^{-1}$) to separate the EXAFS contributions from different coordination shells. To obtain the quantitative structural

parameters around central atoms, least-squares curve parameter fitting was performed using the ARTEMIS module of IFEFFIT software packages.

1.6. Post-characterizations

The coated hybrid after durability test was also collected for post-characterization.

1.7. Al-air battery tests

A homemade Al-air cell was established to test the practical performance of this catalyst. The electrochemical properties of the Al-air cells with this cathode catalyst were measured by LANBTS. A polished and washed Al disc (4N, Alfa Aesar) worked as the metal electrode; $Co_{0.85}$Se@N,Se-CNFs served in the opposite electrode; 7 M KOH aqueous solution (40 mL) filled between them. The surface area of the electrodes exposing to the liquid was designed to be 1 cm^2. To prepare this cathode, nickel foam was cut into discs and loaded the catalytic layer (CL) facing the liquid and the gas diffusion layer (GDL) on the back facing air. To obtain CL, $Co_{0.85}$Se@N,Se-CNFs (85 mg) was ground with active carbon (85 mg) and Ketjen black (25 mg). This mixture was dropped to 15 mL of ethanol with polytetrauoro-ethylene emulsion (PTFE, 5 wt. %, 380 μL). After this solution concentrated into a soft paste, it was smeared on one side of the nickel foam disc and pressed at 1.5 MPa. For GDL, Ketjen black (55 mg) and activated carbon (35 mg) were ground together and poured with 160 mg PTFE (60 wt. %) into ethanol before coating on the disc. Finally, air cathodes were dried at 90°C before sintering at 340 °C for 1 h in Ar.

These Al-air cells were measured by constant discharge current of 50 mA cm^{-2} or dynamic galvanostatic current (30 min per part). The specific capacity of metal electrodes were defined as:

$$\text{Specific capacity} = It/\Delta m \quad (7)$$

where I symbolizes discharging current (A cm^{-2}), Δm signifies weight loss of this aluminum

plate(g), and t describes the working duration (s).

The power density of the Al-air battery could be calculated by the following formula:

$$P = V \times I \quad (8)$$

where P symbolizes the power density (W cm^{-2}), V signifies the discharging voltage (V) and I describes the corresponding discharging current density (A cm^{-2}).

1.5. C_{dl} measuring

The electrochemical double-layer capacitances (C_{dl}) was characterized by testing the capacitive current associated with double-layer charging from CV scanning between -0.2 V to -0.1 V versus Ag/AgCl (3.5 M KCl) in 0.1 M Na_2SO_4 solution[2]. The scanning rates were set as 20, 30, 50, 80, 100, 130, 150, 180, 200 mV s^{-1}. The C_{dl} was calculated through plotting the $\triangle i = (i_a - i_b)$ at -0.15 V versus Ag/AgCl against the scanning rate, where the C_{dl} was half of the slope.

The potential value vs reversible hydrogen electrode (RHE) was calculated from the referred potential vs Ag/AgCl by the formula:

$$E_{(RHE)} = E_{(Ag/AgCl)} + E^{\theta}_{(Ag/AgCl)} + 0.0591 \times pH \quad (9)$$

where pH relates to the 3.5 M Ag/AgCl solution and $E^{\theta}_{(Ag/AgCl)}$ symbolizes the standard potential of Ag/AgCl/3.5 M KCl at RT (0.2046 V vs. RHE).

2. DFT study

2.1 The thermodynamics of the ORR

The ORR activities on active sites of heteroatom-doped defective graphene were studied in detail. In alkaline environment, the oxygen molecular could be reduction to OH^-, and the detail reaction scheme is shown as below:

$$O_2\,(g) + H_2O\,(l) + e^- + * \rightarrow OOH^* + OH^- \quad (1)$$

$$OOH^* + e^- \rightarrow O^* + OH^- \quad (2)$$

$$O^* + H_2O\ (l) + e^- \rightarrow OH^* + OH^- \quad (3)$$

$$OH^* + e^- \rightarrow * + OH^- \quad (4)$$

where * refers to the active site. (l) and (g) refer to the liquid and gas phases, respectively. *O, *OH and *OOH are the adsorbed intermediates.

For each step, the reaction free energy ΔG is defined as the difference between free energies of the initial and final states and is given by the expression,

$$\Delta G_1 = \Delta G_{OOH^*} - 4.92 + \Delta G(\mathrm{pH}) + eU \quad (5)$$

$$\Delta G_2 = \Delta G_{O^*} - \Delta G_{OOH^*} + \Delta G(\mathrm{pH}) + eU \quad (6)$$

$$\Delta G_3 = \Delta G_{OH^*} - \Delta G_{O^*} + \Delta G(\mathrm{pH}) + eU \quad (7)$$

$$\Delta G_4 = -\Delta G_{OH^*} + \Delta G(\mathrm{pH}) + eU \quad (8)$$

The free energy of each step was calculated using Equation 9, and the reaction free energy was given as the difference between the initial and final states:

$$\Delta G = \Delta E_{DFT} + \Delta E_{ZPE} - T\Delta S + \Delta G_U + \Delta G_{pH} + \Delta G_E \quad (9)$$

where E_{DFT} is the reaction energy calculated by DFT, E_{ZPE} is the zero-point energy, T is the temperature at 298 K, S is the entropy, and $\Delta G_U = -eU$ is the free energy term introduced by changing the electrode potential U. In addition, $\Delta G_{\mathrm{pH}} = -2.303 k_{\mathrm{b}} T \times \mathrm{pH}$. ΔG_{E} represents the electrical double-layer effect at the electrode surface, but it is usually ignored because of its small value. Based on previous experience, the entropy S of the species in the gas phase involved in the calculations was obtained from the National Institute of Standards and Technology (NIST). In addition, to improve the accuracy of the DFT calculations, we used standard data for correction; i.e., the O_2 free energy was calculated from the reaction $O_2 + 2H_2 = 2H_2O$, for which ΔG is 4.92 eV at 298 K and

0.035 bar. The absorption energies were calculated as follows, $\Delta E_{OH*} = E(OH*) - E(*) - (E_{H2O} - 1/2E_{H2})$, $\Delta E_{OOH*} = E(OOH*) - E(*) - (2E_{H2O} - 3/2E_{H2})$, $\Delta E_{O*} = E(O*) - E(*) - (E_{H2O} - E_{H2})$, E_{H2O} and E_{H2} are the calculated DFT energies of H_2O and H_2 molecules in the gas phase using the approaches outlined by Nørskov et al. DZPE and TDS are the zero point energy difference and the entropy change between the absorbed state and the free state, i.e., the gas phase, respectively, and T is the temperature (298.15 K in this work).

2.2 Computational details

Density functional theroy (DFT) calculations can provide insight into predicting the ORR activity of a structure.[3-5] In this study, we performed adsorption calculations using a 6×6 supercell of graphene. Spin-polarized DFT calculations were performed using the Vienna ab initio simulation package (VASP).[6] Core electrons were processed using the projector augmented wave[7] and generalized gradient approximation[8] exchange-correlation effects according to the Perdew–Burke–Ernzerhof functional.[9] The kinetic energy cutoff was 520 eV, and the convergence tolerances for residual force and energy were set to 0.01 eV/Å and 10^{-5} eV, respectively, on each atom. A 3×3×1 k-mesh grid was used for geometry optimization, and a 7×7×1 k-mesh grid was used for electronic structure calculations. The vacuum layer thickness in the *z*-direction was set to 20 Å to avoid artificial interactions between periodic images. In the DFT calculations, we performed DFT-D3 empirical correction of van der Waals interactions[10] because these interactions between intermediates and the surface can determine the stability of the adsorbed intermediate and thus the optimal conditions.

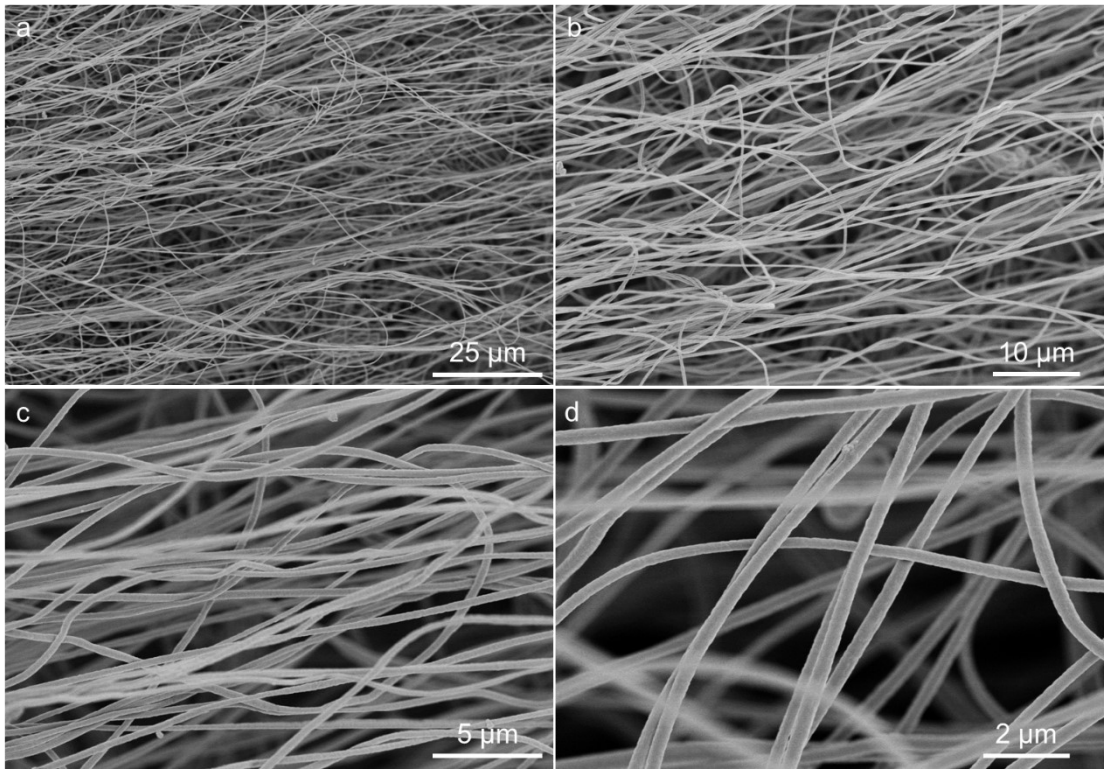

Fig. S1. (a-d) SEM images of raw electrospun PAN nanofibers with different magnifications.

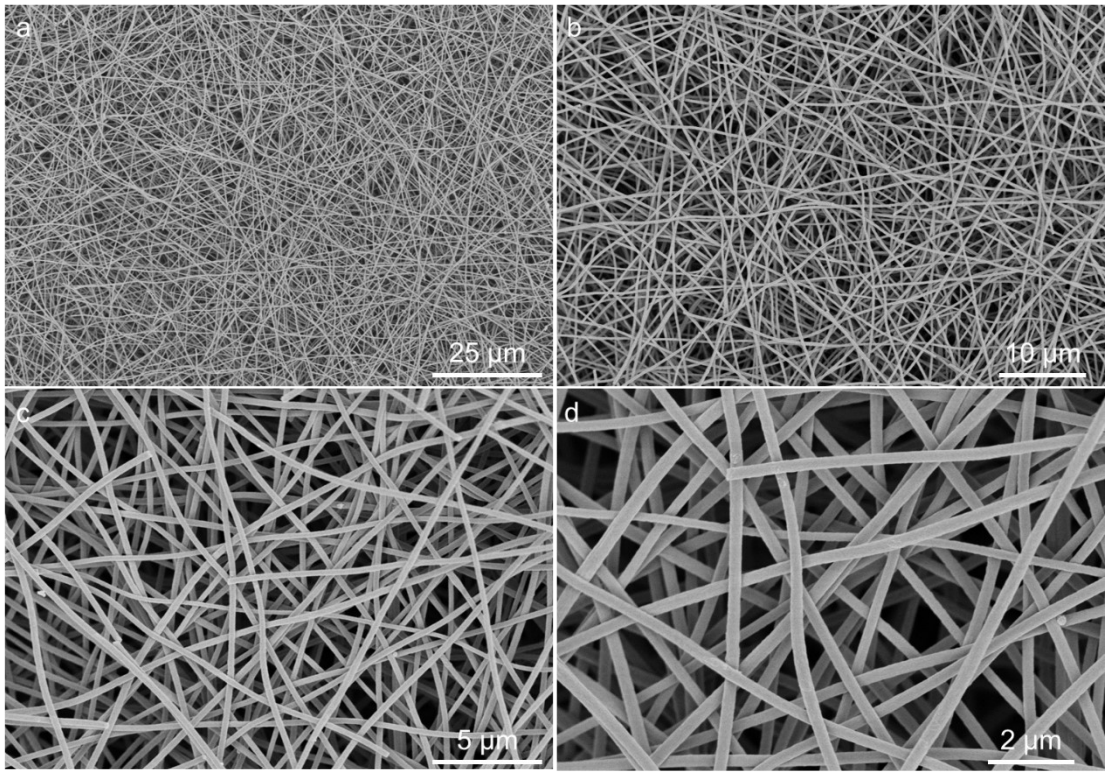

Fig. S2. (a-d) SEM images of N,Se-CNFs carbonized from the raw mat and Se powder with different magnifications.

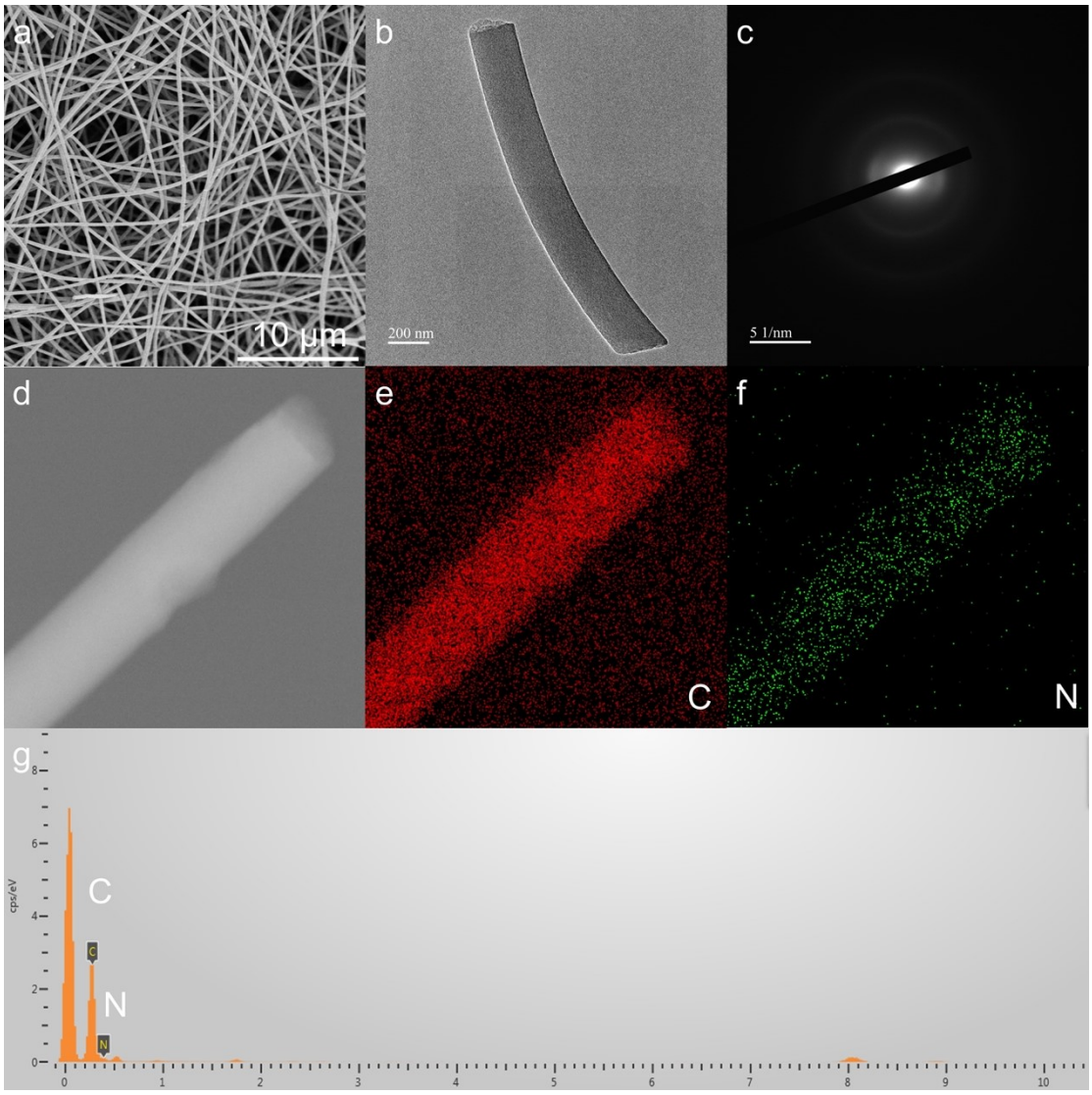

Fig. S3. (a-b) SEM(a) and TEM(b) image of N-CNFs carbonized from the raw mat without Se powder. (c) SAED patterns of N-CNFs. (d-f) STEM image(d) and the corresponding elemental mapping images of N-CNFs: C(e) and N(f) species. (g) EDS analysis of N-CNFs.

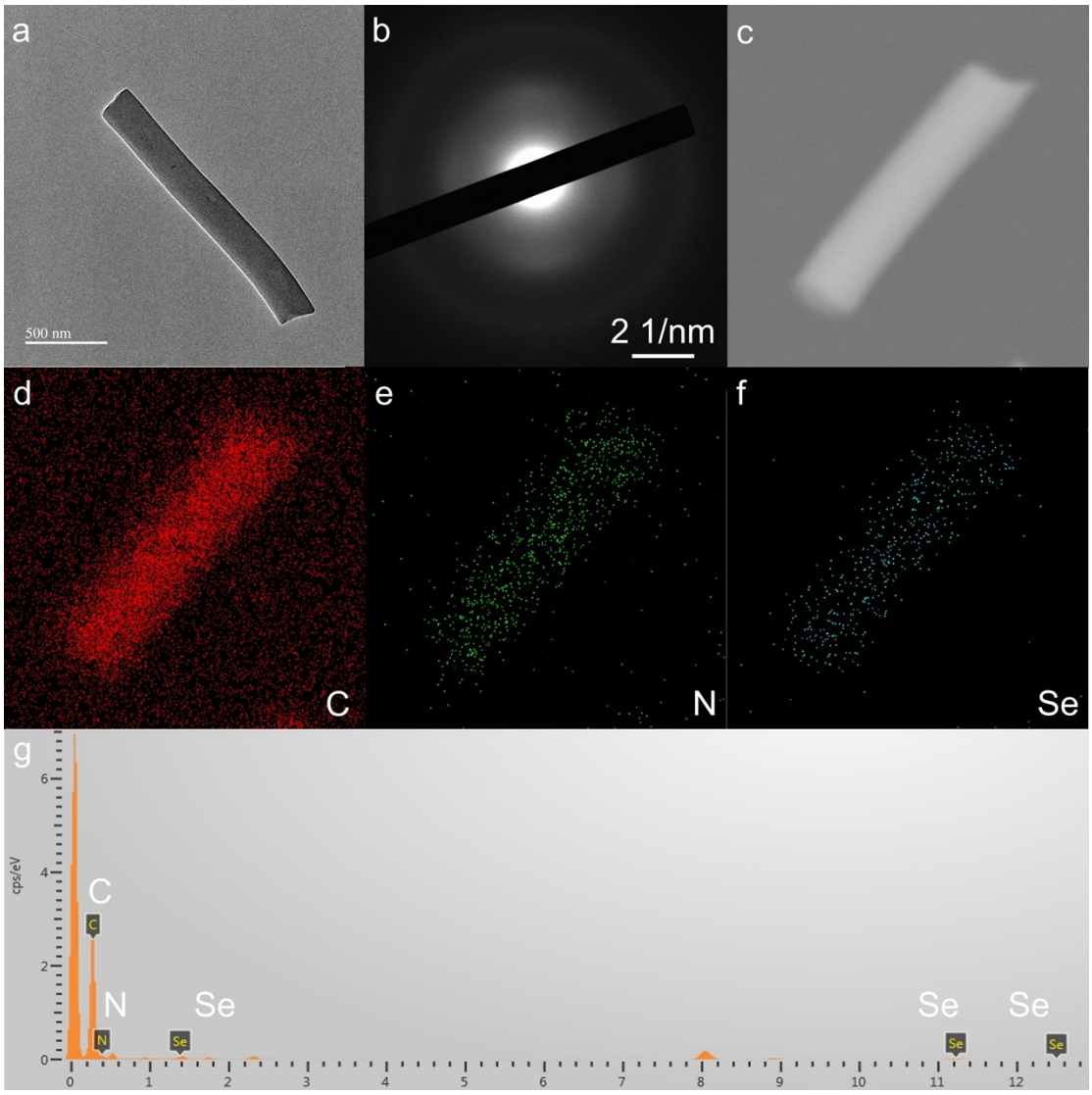

Fig. S4. (a) TEM image of N,Se-CNFs carbonized from the raw mat with Se powder. (b) SAED patterns of N,Se-CNFs. (c-f) STEM image(c) and the corresponding elemental mapping images of N,Se-CNFs: C(d), N(e) and Se(f) species. (g) EDS analysis of N,Se-CNFs.

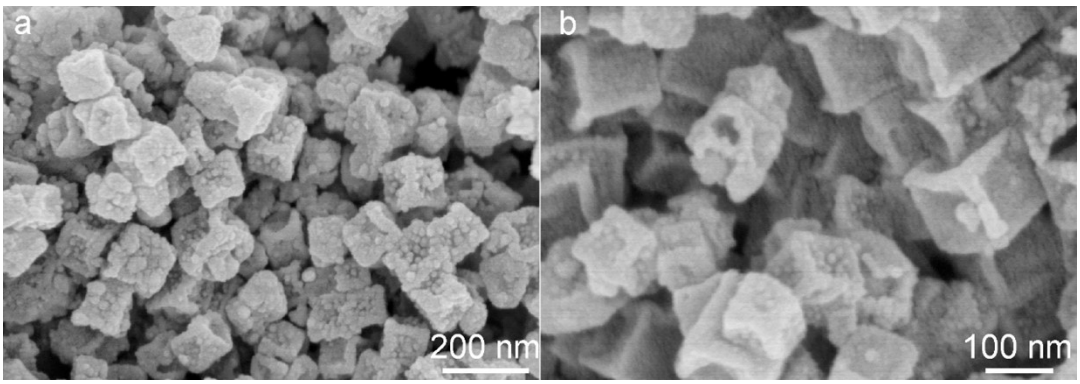

Fig. S5. (a and b) SEM images of $Co_{0.85}Se$/C carbonized from ZIF-67 nanocubes and Se powder with different magnifications.

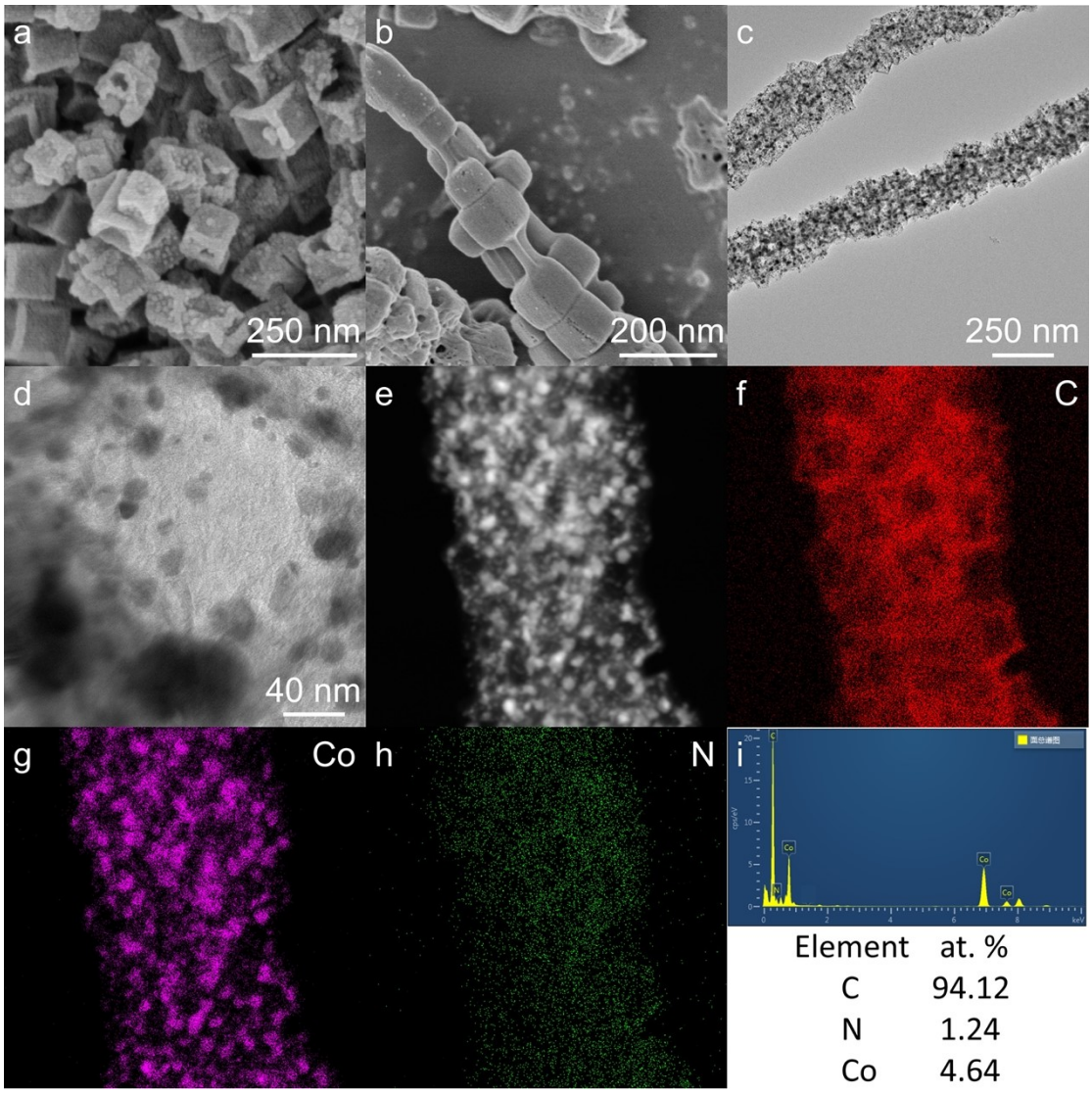

Fig. S6. (a) SEM image of Co/C carbonized from ZIF-67 nanocubes. (b-d) SEM(b) and TEM(c) images of Co@N-CNFs carbonized from electrospun ZIF-67 nanocubes with Co nanoparticles(d) in the carbon matrix. (e-h) STEM image(e) and the corresponding elemental mapping images of Co@N-CNFs: C(f), Co(g) and N(h) species. (i) EDS analysis of Co@N-CNFs with a table of the composition content.

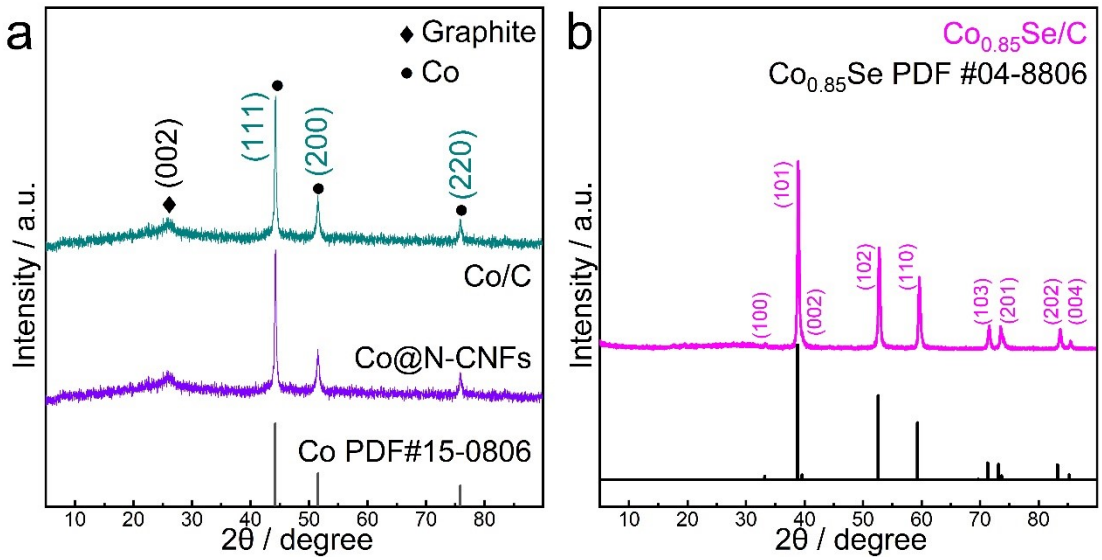

Fig. S7. XRD patterns of Co/C carbonized from only ZIF-67 nanocubes and Co@N-CNFs from electrospun ZIF-67 nanocubes(a), and $Co_{0.85}Se$/C carbonized from ZIF-67 nanocubes with Se powder(b).

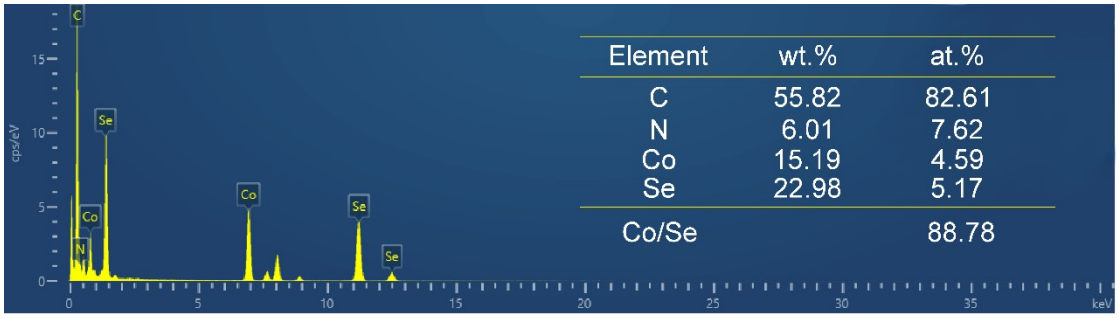

Fig. S8. EDS analysis of $Co_{0.85}Se$@N,Se-CNFs with a table of the composition content.

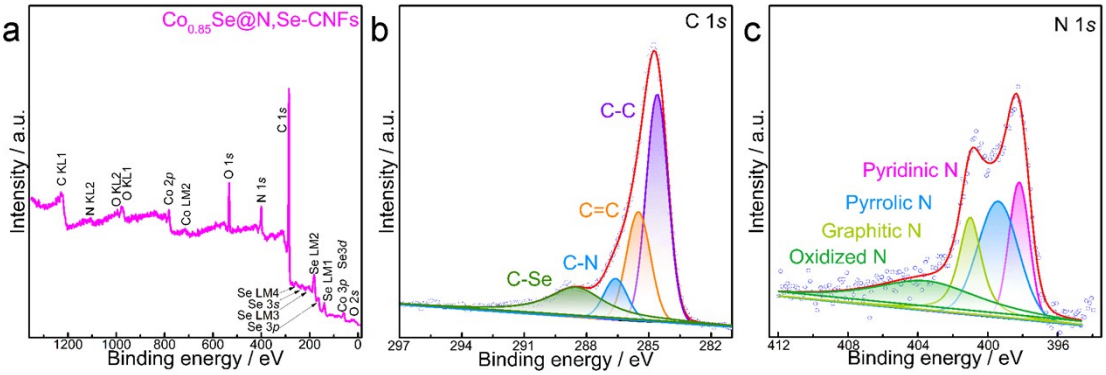

Fig. S9. (a) XPS spectra of $Co_{0.85}Se$@N,Se-CNFs. (b) The high-resolution spectra of C 1*s*. (c) The high-resolution spectra of N 1*s*.

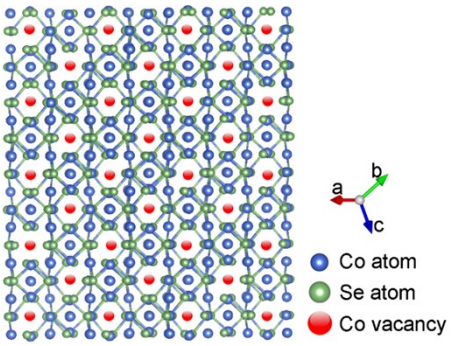

Fig. S10. Crystal model of $Co_{0.85}Se$ showing the ordered cation vacancies.

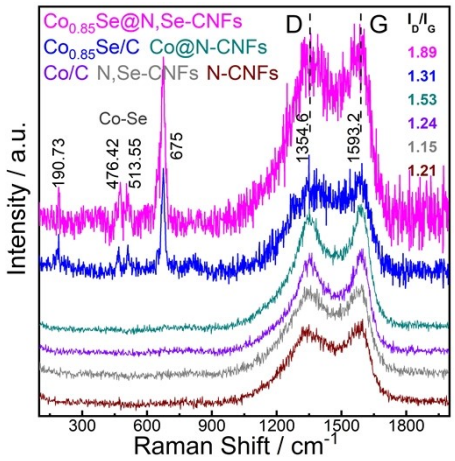

Fig. S11. Raman spectra of $Co_{0.85}Se$@N,Se-CNFs, $Co_{0.85}Se$/C, Co@N-CNFs, Co/C, N,Se-CNFs and N-CNFs.

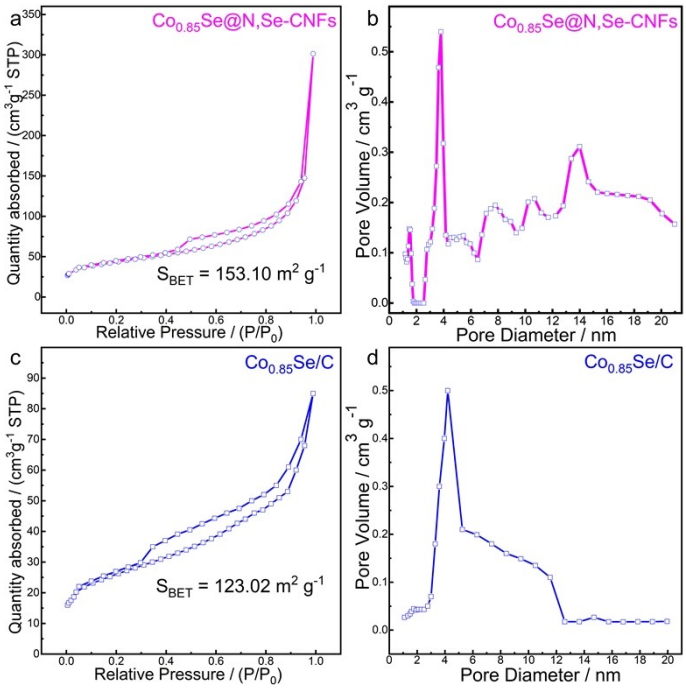

Fig. S12. N_2 adsorption-desorption isotherms of $Co_{0.85}Se$@N,Se-CNFs(a) and $Co_{0.85}Se$/C(c) the pore size distribution curves from the BJH model(b and d).

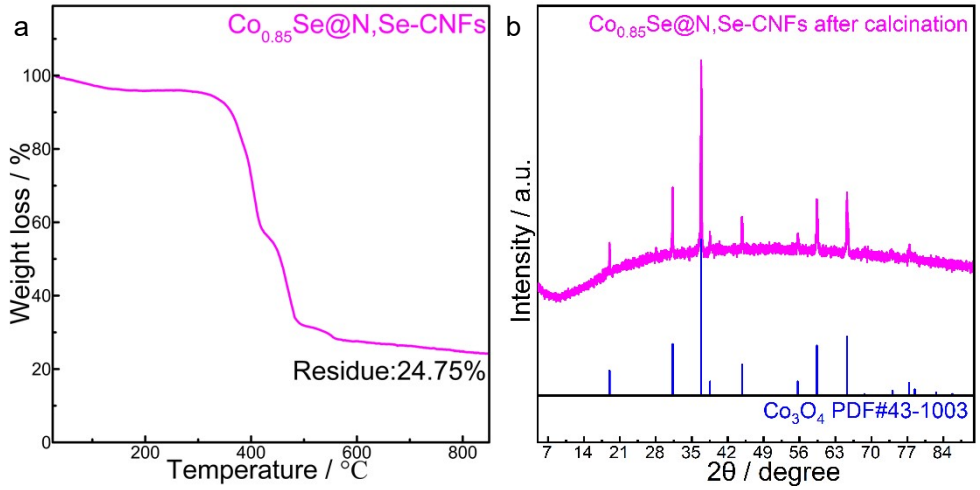

Fig. S13. (a and b) TGA curve of $Co_{0.85}Se$@N,Se-CNFs calcinated in air(a) and XRD patterns of the corresponding product(b).

Thermal decomposition of $Co_{0.85}Se$@N,Se-CNFs was also evaluated by thermogravimetric analysis (TGA) as shown in Fig. S13a. The initial mass loss of this catalyst in air lay under 300 ℃, originating maybe from the release of adsorbed hydrogen oxide and other small molecules. After multiple steps of thermal reactions, $Co_{0.85}Se$ finally evolved into Co_3O_4, determined by the XRD patterns of the final product displayed in Fig. S13b. In conclusion, this process included mainly the combustion of carbon skeleton and a series reactions between $Co_{0.85}Se$ and oxygen to finally form Co_3O_4 ($Co_{0.85}Se$ + carbon matrix → carbon dioxide + gas contain Se + Co_3O_4). The residue weight of the final Co_3O_4 (24.75 wt. %) relates to the content of $Co_{0.85}Se$ in $Co_{0.85}Se$@N,Se-CNFs (13.26 wt. %).

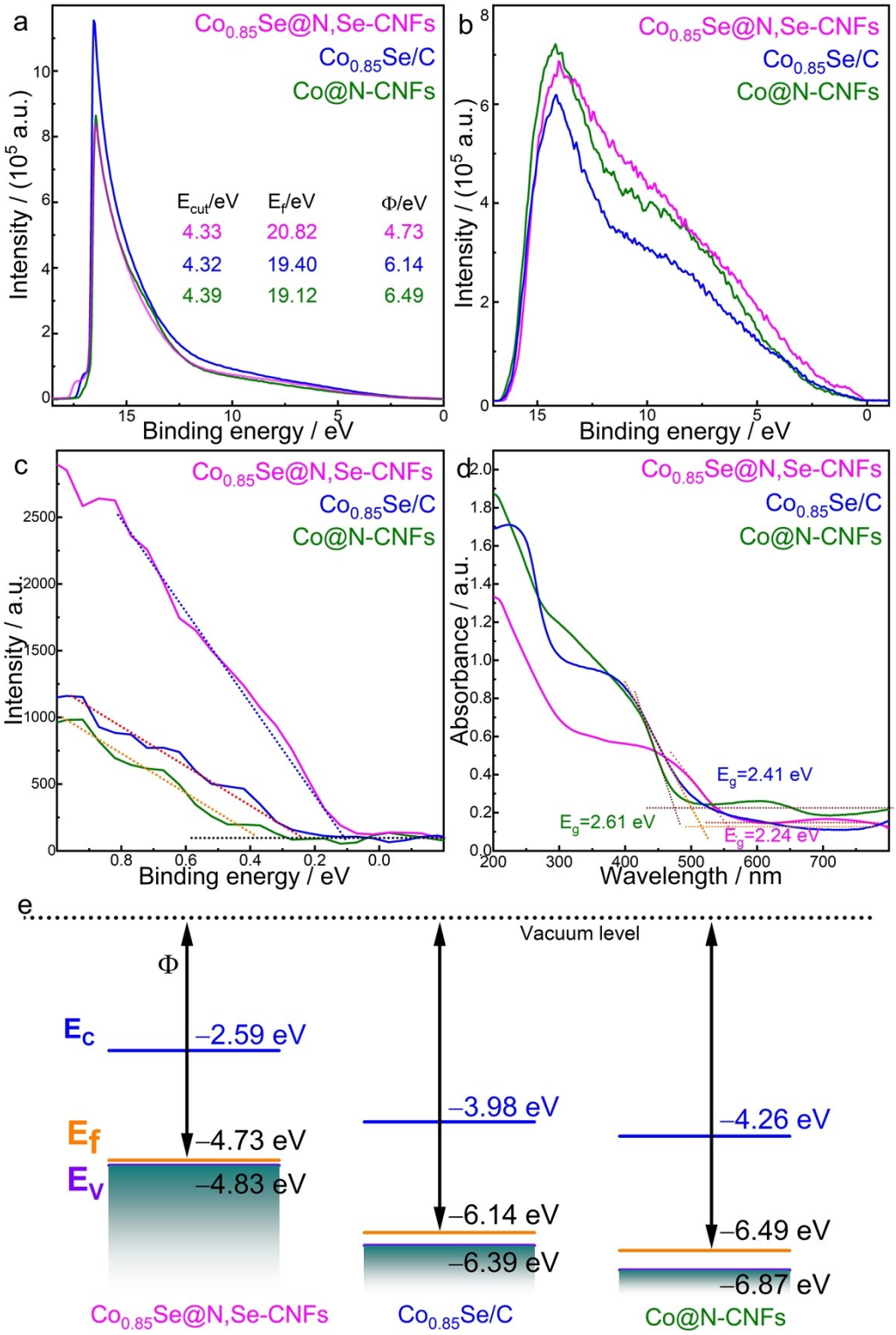

Fig. S14. (a-b) The ups spectra of $Co_{0.85}Se$@N,Se-CNFs, $Co_{0.85}Se$/C and Co@N-CNFs with the applied bias voltage of -5 V(a) and 0 V(b). (c) The magnified ups spectra from b. (d) UV−vis absorption spectra of $Co_{0.85}Se$@N,Se-CNFs, $Co_{0.85}Se$/C and Co@N-CNFs. (e) Energy diagram showing the electronic band structure(conduction band, valence band and Fermi level) of $Co_{0.85}Se$@N,Se-CNFs, $Co_{0.85}Se$/C and Co@N-CNFs.

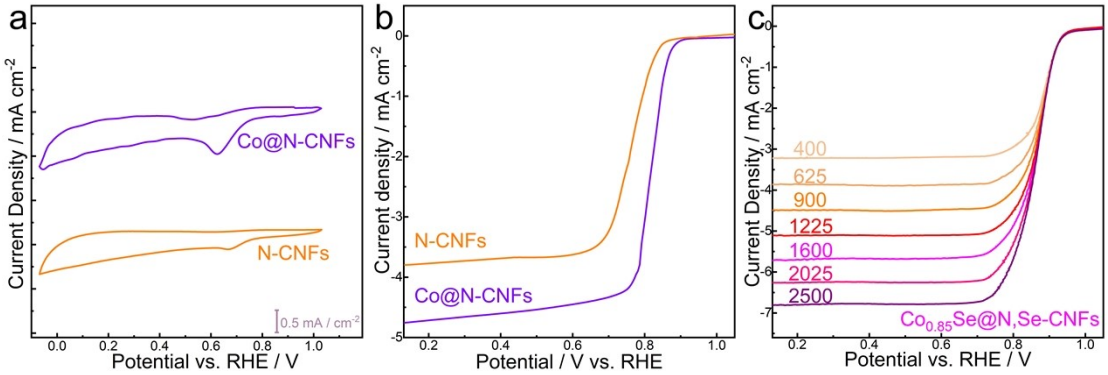

Fig. S15. (a) CV curves of Co@N-CNFs and N,Se-CNFs. (b) LSV curves of Co@N-CNFs and N-CNFs at a rotating speed of 1600 rpm. (c) LSV curves of $Co_{0.85}$Se@N,Se-CNFs recorded at rotating speeds from 400 to 2500 rpm.

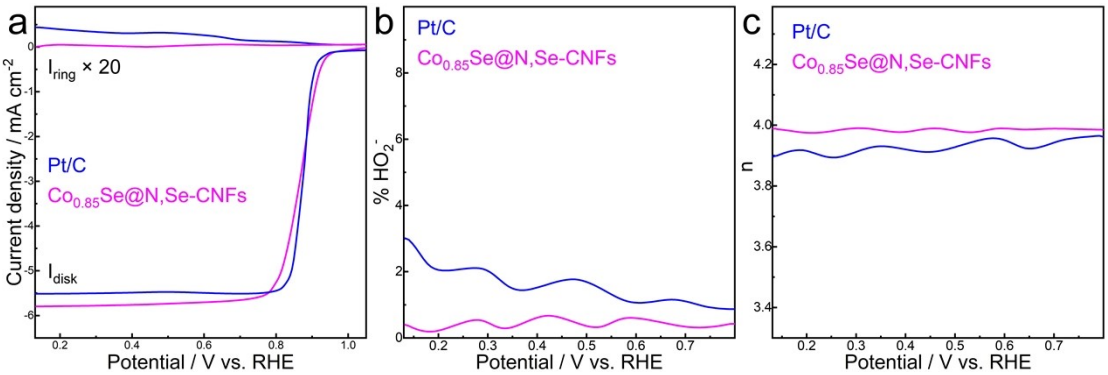

Fig. S16. (a) Rotating ring-disk electrode voltammograms of $Co_{0.85}$Se@N,Se-CNFs and Pt/C on glassy carbon electrodes in O_2-saturated 0.1 M KOH solution with a rotation rate of 1600 rpm. (b) Percentage of HO_2^-/H_2O_2 of $Co_{0.85}$Se@N,Se-CNFs and Pt/C at different potentials based on the corresponding RRDE data. (c) The electron transfer number (n) of $Co_{0.85}$Se@N,Se-CNFs and Pt/C at different potentials based on the corresponding RRDE data.

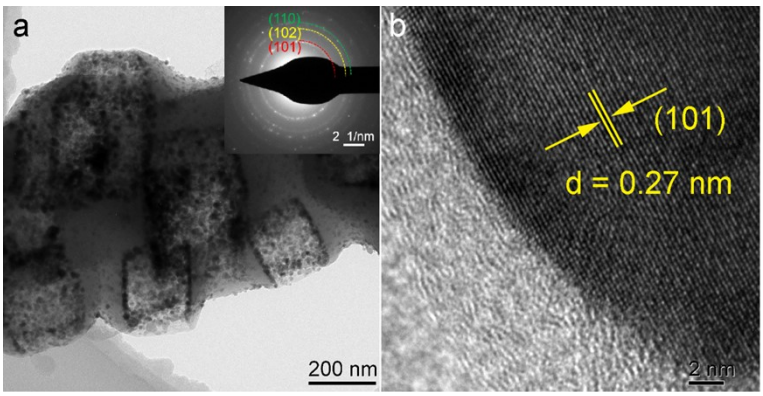

Fig. S17. (a) TEM image $Co_{0.85}$Se@N,Se-CNFs after long-term catalytic durability test, the inset of (a) shows the corresponding SAED patterns. (b) The corresponding HRTEM image.

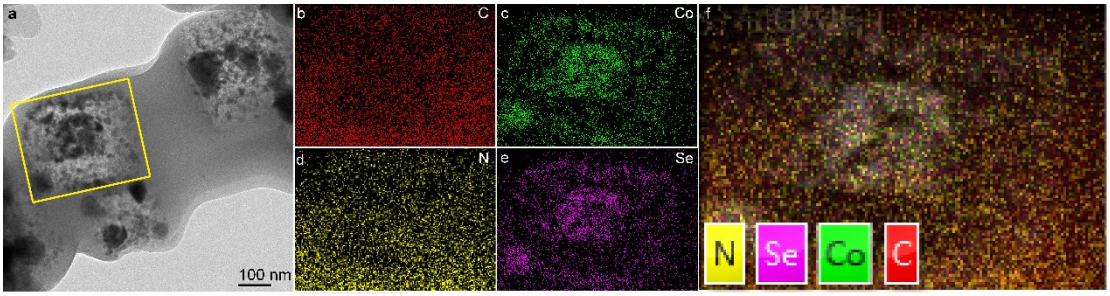

Fig. S18. (a-e) STEM image of $Co_{0.85}Se$@N,Se-CNFs after long-term catalytic durability test (a) and the elemental mapping of C(b), Co(c), N(d) and Se(e) of the selected area. (f) The comprehensive elemental distribution mapping.

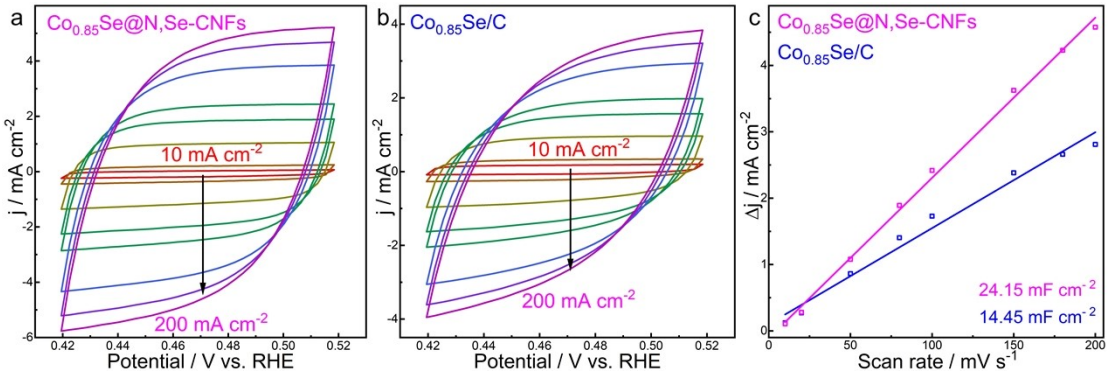

Fig. S19. (a-c) Cyclic voltammetry curves of $Co_{0.85}Se$@N,Se-CNFs(a) and $Co_{0.85}Se$/C(b) and charging current density differences plotted against scan rates of the as-prepared samples(c).

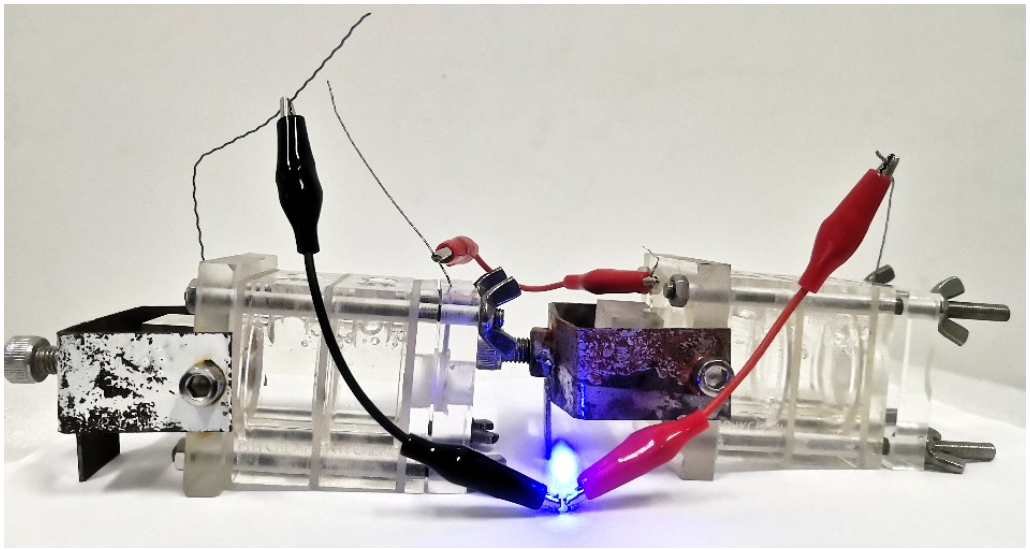

Fig. S20. A digital photo of LED charged by $Co_{0.85}Se$@N,Se-CNFs equipped Al-air batteries.

Table S1. EXAFS fitting parameters at the Co K-edge for $Co_{0.85}Se$@N,Se-CNFs.

Sample	Shell	N [a]	R (Å) [b]	σ^2 (Å$^2\cdot10^{-3}$) [c]	ΔE_0 (eV) [d]	*R* factor (%)
	Co-O	1.7	1.92	9.8	-8.2	0.4
	Co-Se	2.9	2.39	7.5	-8.2	

[a] *N*: coordination numbers; [b] *R*: bond distance; [c] σ^2: Debye-Waller factors; [d] ΔE_0: the inner potential correction. *R* factor: goodness of fit. S_0^2 was set as 0.86 for Co-O/Se, which was obtained from the experimental EXAFS fit of reference $CoSe_x$ by fixing CN as the known crystallographic value and was fixed to all the samples.

Table S2. EXAFS fitting parameters at the Se K-edge for $Co_{0.85}Se$@N,Se-CNFs.

Sample	Shell	N [a]	R (Å) [b]	σ^2 (Å$^2\cdot10^{-3}$) [c]	ΔE_0 (eV) [d]	*R* factor (%)
	Se-Co	2.8	2.43	7.6	8.7	0.8

[a] *N*: coordination numbers; [b] *R*: bond distance; [c] σ^2: Debye-Waller factors; [d] ΔE_0: the inner potential correction. *R* factor: goodness of fit. S_0^2 was set as 0.86 for Se-Co, which was obtained from the experimental EXAFS fit of reference $CoSe_x$ by fixing CN as the known crystallographic value and was fixed to all the samples.

Table S3. Summary of ORR activities of Co-based catalysts.

ORR catalyst	Onset potential (V vs. RHE)	Half-wave potential (V vs. RHE)	Platform current density (mA cm^{-2})	Refs
$Co_{0.85}Se$@N,P-CNFs	0.933	0.868	5.72	This work
$Co_{0.85}Se$ /C	0.898	0.827	4.53	This work
N,Se-CNFs	0.840	0.755	3.96	This work
Pt/C	0.921	0.870	5.65	This work
$Co_{0.85}Se$@CNFs	0.9	0.82	5.0	[11]
$Ni_{0.85}Se$–NHCS	0.85	~0.71	4.35	[12]
$Co_{0.85}Se$-NHCS	0.89	0.76	4.67	[13]
$Ni_{0.85}Se/Co_{0.85}Se$-NHCS-2	0.9	0.77	4.66	[13]
$CoSe_2$@NC	0.904	0.83	5.79	[14]
Cu-14-Co_3Se_4/GC	0.892	0.782	~5.0	[15]
$CoSe_2$/GC	0.830	0.686	~4.1	[15]
Co–Fe–P–Se/NC	~0.89	0.76	~4.1	[16]
$(Ni,Co)Se_2$	0.82	0.70	4.00	[17]
Se-rGO	0.863	0.740	~4.44	[18]
$CoSe_2$/rGO	0.901	0.721	~4.55	[18]
$CoSe_2$/Se-rGO	0.903	0.803	~4.9	[18]
B-$CoSe_2$@CoNi LDH	0.904	0.81	~5.8	[19]

Table. S4. Summary of the series resistance (R_s) and charge-transfer resistance (R_{ct}) of various ORR catalysts

Cathode catalyst	R_s/Ω	R_{ct}/Ω	Refs
$Co_{0.85}Se$@N,Se-CNFs	65.84	11.5	This work
$Co_{0.85}Se$/C	64.87	48.32	This work
N,Se-CNFs	65.56	232.90	This work
$Co_{0.85}Se$	-	172.1	[20]
$Ni_{0.85}Se$-NHCS	-	14.82	[12]
$Ni_{0.95}Se$-NHCS	-	17.79	[12]
NiSe-NHCS	-	21.22	[12]
$CoSe_2$-$SnSe_2$/CNT	9.9	39	[21]
$CoSe_2$-$SnSe_2$	10.4	1093	[21]
o-$CoSe_2$|P	-	2.2	[22]
Annealed c-$CoSe_2$	-	19.7	[22]
c-$CoSe_2$	-	7930	[22]
$Co_{0.85}Se$	13.6	228	[23]
$Co_{0.85}Se$/graphene network	9.3	177	[23]
NC-$Co_{0.85}Se$	-	86.3	[24]
H-$Co_{0.85}Se$	-	198.7	[24]
$CoSe_2$–CNT	-	10.9	[25]
$CoSe_2$ powders	-	29.3	[25]
$Co_{0.85}Se$@CNWs	-	39	[26]
$Co_{0.85}Se$ NWs	-	508	[26]
Bare $Co_{0.85}Se$	-	262.6	[27]
$Co_{0.85}Se$@NG_3	-	35.62	[27]

References

[1] Wang Junren, Lu Huimin, Hong Qingshui, et al. Porous N,S-codoped carbon architectures with bimetallic sulphide nanoparticles encapsulated in graphitic layers: Highly active and robust electrocatalysts for the oxygen reduction reaction in Al-air batteries[J]. Chemical Engineering Journal. 2017, 330:1342-1350.

[2] Gao Shan, Sun Zhongti, Liu Wei, et al. Atomic layer confined vacancies for atomic-level insights into carbon dioxide electroreduction[J]. Nature Communcations. 2017, 8:14503.

[3] Li Mufan, Zhao Zipeng, Cheng Tao, et al. Ultrafine jagged platinum nanowires enable ultrahigh mass activity for the oxygen reduction reaction[J]. Science. 2016, 354(6318): 1414.

[4] Bu Lingzheng, Zhang Nan, Guo Shaojun, et al. Biaxially strained PtPb/Pt core/shell nanoplate boosts oxygen reduction catalysis[J]. Science. 2016, 354(6318): 1410.

[5] Huang Xiaoqing, Zhao Zipeng, Cao Liang, et al. High-performance transition metal-doped Pt/Ni octahedra for oxygen reduction reaction[J]. Science. 2015, 348(6240): 1230.

[6] Kresse G., Furthmüller J. Efficient iterative schemes for ab initio total-energy calculations using a plane-wave basis set[J]. Physical Review B. 1996, 54(16): 11169-11186.

[7] Blöchl P. E. Projector augmented-wave method[J]. Physical Review B. 1994, 50(24): 17953-17979.

[8] Perdew John P., Wang Yue. Accurate and simple analytic representation of the electron-gas correlation energy[J]. Physical Review B. 1992, 45(23): 13244-13249.

[9] Perdew John P., Burke Kieron, Ernzerhof Matthias. Generalized gradient approximation made simple[J]. Physical Review Letters. 1996, 77(18): 3865-3868.

[10] Lee Kyuho, Murray Eamonn D., Kong Lingzhu, et al. Higher-accuracy van der Waals density functional[J]. Physical Review B. 2010, 82(8): 081101.

[11] Gui Liangqi, Huang Ziliang, Ai Ding, et al. Integrated ultrafine $Co_{0.85}Se$ in carbon nanofibers: an efficient and robust bifunctional catalyst for oxygen electrocatalysis[J]. Chemistry. 2019, 26:4063-4069.

[12] Pan Qiuren, Li Sijie, Tong Kaixin, et al. Engineering Ni^{3+} inside nickel selenide as efficient bifunctional oxygen electrocatalysts for Zn-air batteries[J]. Journal of Materials Science. 2019, 54(12): 9063-9074.

[13] Peng Lijuan, Huang Jieping, Pan Qiuren, et al. A simple method for the preparation of a nickel selenide and cobalt selenide mixed catalyst to enhance bifunctional oxygen activity for Zn–air batteries[J]. RSC Advances. 2021, 11(32): 19406-19416.

[14] Ding Kuixing, Hu Jiugang, Luo Jia, et al. Confined N-$CoSe_2$ active sites boost bifunctional oxygen electrocatalysis for rechargeable Zn–air batteries[J]. Nano Energy. 2022, 91 106675.

[15] Dai Jiale, Zhao Dengke, Sun Wenming, et al. Cu(II) ions induced structural transformation of cobalt selenides for remarkable enhancement in oxygen/hydrogen electrocatalysis[J]. ACS Catalysis. 2019, 9(12): 10761-10772.

[16] Wu Hengbo, Wang Jie, Yan Ji, et al. MOF-derived two-dimensional N-doped carbon nanosheets coupled with Co-Fe-P-Se as efficient bifunctional OER/ORR catalysts[J]. Nanoscale. 2019, 11(42): 20144-20150.

[17] Sun Changqi, Guo Xiaosong, Zhang Jingyan, et al. Rechargeable Zn-air batteries initiated by nickel–cobalt bimetallic selenide[J]. Journal of Energy Chemistry. 2019, 38:34-40.

[18] Zhao Yuan, Zhang Chuanxiang, Fan Rong, et al. Selenium Decorated Reduced Graphene Oxide Supported $CoSe_2$ Nanoparticles as Efficient Electrochemical Catalyst for the Oxygen Reduction Reaction[J]. ChemElectroChem. 2018, 5(21): 3287-3292.

[19] Song Junnan, Chen Ying, Huang Hongjiao, et al. Heterointerface engineering of hierarchically assembling layered double hydroxides on cobalt selenide as efficient trifunctional electrocatalysts for

water splitting and zinc-air battery[J]. Advanced Science. 2022:e2104522.
[20] Li Siwen, Peng Sijia, Huang Linsong, et al. Carbon-coated Co^{3+}-rich cobalt selenide derived from ZIF-67 for efficient electrochemical water oxidation[J]. ACS Appl Mater Interfaces. 2016, 8(32): 20534-20539.
[21] Yu Bo, Qi Fei, Zheng Binjie, et al. Self-assembled pearl-bracelet-like $CoSe_2$-$SnSe_2$/CNT hollow architecture as highly efficient electrocatalysts for hydrogen evolution reaction[J]. Journal of Materials Chemistry A. 2018, 6(4): 1655-1662.
[22] Zheng Yarong, Wu Ping, Gao Minrui, et al. Doping-induced structural phase transition in cobalt diselenide enables enhanced hydrogen evolution catalysis[J]. Nat Commun. 2018, 9(1): 2533.
[23] Yu Bo, Qi Fei, Chen Yuanfu, et al. Nanocrystalline $Co_{0.85}Se$ anchored on graphene nanosheets as a highly efficient and stable electrocatalyst for hydrogen evolution reaction[J]. ACS Applied Materials Interfaces. 2017, 9(36): 30703-30710.
[24] Yu Bo, Qi Fei, Wang Xinqiang, et al. Nanocrystalline $Co_{0.85}Se$ as a highly efficient non-noble-metal electrocatalyst for hydrogen evolution reaction[J]. Electrochimica Acta. 2017, 247:468-474.
[25] Kim Jin Koo, Park Gi Dae, Kim Jung Hyun, et al. Rational design and synthesis of extremely efficient macroporous $CoSe_2$-CNT composite microspheres for hydrogen evolution reaction[J]. Small. 2017, 13(27).
[26] Sun Baochen, Wang Xinqiang, Yang Dongxu, et al. Self-assembled $Co_{0.85}Se$/carbon nanowires as a highly effective and stable electrocatalyst for the hydrogen evolution reaction[J]. RSC Advances. 2019, 9(30): 17238-17245.
[27] Wang Haiqi, Wang Xinqiang, Yang Dongxu, et al. $Co_{0.85}Se$ hollow nanospheres anchored on N-doped graphene nanosheets as highly efficient, nonprecious electrocatalyst for hydrogen evolution reaction in both acid and alkaline media[J]. Journal of Power Sources. 2018, 400:232-241.